

Self-driven real-time angle vector sensor as security dialer based on bi-directional backstop triboelectric nanogenerator



Wenchi Hou ^{a,b}, Xiaolong Tang ^a, Lin Fang ^a, Qiwei Zheng ^{a,b}, Xiangyu Chen ^{b,*}, Li Zheng ^{a,*}

^a College of Mathematics and Physics, Shanghai Key Laboratory of Materials Protection and Advanced Materials in Electric Power, Shanghai University of Electric Power, Shanghai 200090, PR China

^b CAS Center for Excellence in Nanoscience, Beijing Key Laboratory of Micro-nano Energy and Sensor, Beijing Institute of Nanoenergy and Nanosystems, Chinese Academy of Sciences, Beijing 100083, PR China

ARTICLE INFO

Keywords:

Internet of Things
Angle vector sensor
Triboelectric nanogenerator
Bi-directional backstop
Real-time monitoring

ABSTRACT

With the developments of Internet of Things (IoT), there is an endless demand for various sensors that can maintain a certain level of functional performance while providing excellent energy consumption levels, preferably harvesting energy from the environment. In this work, we designed a self-driven angle vector sensor based on triboelectric nanogenerator (TENG) for constructing a reliable and low-cost IoT sensing system. Based on the high signal-to-noise (SNR) output of rotary TENG, a bi-directional backstop TENG (BB-TENG) is designed to realize direct quantization process of rotation angle and direction in real time. The homemade BB-TENG can generate an output voltage up to 174.45 V to resist external noise and guarantee the measurement quality, furthermore, the maximum speed error of measured rotation speed does not exceed 0.2 rpm. Then, a digital signal processor was implemented to extract the angle vector in real time and presents its application as a passcode dialer. This work not only demonstrates a new strategy in the field of angle measurement, but also extends the application scenario of TENG in the IoT field.

1. Introduction

With the rapid development of information technology, the sensor technology is in great needs and fast evolutions, which is closely related to life and industrial production. As an infrastructure in the field of motion systems, mechanics and fluids, the measurement of rotational angle receives a high level of attention, because the implementation of many functions depends on the angle of rotation [1]. Over the decades, methods for measuring angles have taken various forms and been widely used under different scenarios, such as sensors based on grating structures, giant magnetoresistance effect, electrical effects and electromagnetic induction [2–5]. However, these sensors have a variety of limitations, either requiring continuous external power supply to keep working, or requiring precise manufacturing and processing technology to meet the needs of the assembly, which undoubtedly limits the potential application in large scale and harsh conditions. On the other hand, with the development and combination of network and sensors, Internet of Things (IoT) is rapidly embracing the modern human society. As a promising technology, IoT has gained more and more attention in recent years [6,7]. However, the ubiquitous distributed IoT devices have

brought new problems while empowering society progress. If conventional rotary angle sensors are used as IoT devices that require external power supply to work, which will undoubtedly consume a large amount of power and have a profound negative effect on energy and environment. Therefore, there is an urgent need to design a new type of angle sensor that can generate rotary signals in a self-driven manner.

Recently, triboelectric nanogenerator (TENG) as an efficient approach to harvest environmental energy which derived from Maxwell displacement currents and based on the coupling of triboelectrification effect and electrostatic induction was proposed by Wang's group firstly [8]. TENG has the ability to extensively convert mechanical energy existing in the environment into electricity [9–12] and therefore caught attractive attentions [13–16]. Due to the widespread triboelectric charging effect, TENG can be made from versatile choices of materials and structures, and has the characteristics of high output performance, easy configuration, simple manufacturing, low cost, high scalability and no external power supply [17–19]. In addition, TENG-based systems can also purify airborne particles, which further expands the application of TENG in a wide range of applications [20]. With the advantage of high signal-to-noise ratio (SNR) of TENG [21], various types of TENG-based

* Corresponding authors.

E-mail addresses: chenxiangyu@binn.cas.cn (X. Chen), zhengli@shiep.edu.cn (L. Zheng).

sensors have been researched and developed, such as vibration sensor [22], acoustic sensor [23], wind direction sensor [24], biomechanical sensor [25] and mechanotactile sensor [26]. Notably, there are also many TENG-based rotation sensors reported. In 2018, Choi et al. reported the roller-bearing TENG used to measure angle after Li et al. innovatively created a ball-bearing structure TENG [27,28]. Wu et al. and Li et al. used three or more electrodes to detect the direction of rotation through extracting more movement information [29,30]. Chen et al. achieves a robust speed sensor by reducing damage at the contact electrification interface through changeable mechanical structure [31]. Lu et al. realized the IoT application in driver monitoring field by combining TENG angle sensor with steering wheel [32]. However, the structural complexity of these TENG-based rotation sensors is often ignored, which usually leads to an increase in device size and extra space for motion requirements, thus posing the application challenges of expanding TENG sensors. Moreover, when TENG is used for keypad password input devices, the input process is vulnerable to be attacked through gesture traces, so these security devices also need further improvements [33].

In this work, a real-time angle vector sensor constructed by a bi-directional backstop TENG (BB-TENG) is proposed and demonstrated as a rotary passcode dialer for the first time. This highly integrated BB-TENG device owns the function of measuring both direction and angle of the rotation simultaneously, and it has optimized structural dimensions compared to devices with external backstops [34]. Based on the principles of triboelectrification effect and electrostatic induction, BB-TENG's power generation components are composed of two different materials with opposite electrical polarity and are manufactured using PCB etching technology. The output voltage of BB-TENG can reach 174.45 V, which is sufficient to light 120 LEDs in series as an energy supply. The measurement deviation of the angle sensor based on BB-TENG does not exceed 0.2 rpm, and the sensing output is synchronized with external rotational motion. Finally, BB-TENG is applied to successfully realize a rotary passcode input device, which is integrated with an identity security system to improve the security of the IoT system through an unrepeatable rotation sequence, demonstrating the potential application of TENG as a self-driven sensor and security device in the IoT field.

2. Experimental methods

2.1. Fabrication of the BB-TENG

All components of the bi-directional backstop are modeled first and then fabricated by 3D printer (Flashforge Adventurer 3) using PLA (polylactic acid plastic). The stator panel of TENG is a transparent acrylic board with dimensions of $90 \times 90 \times 3$ mm, a $\Phi 12.2$ mm hole drilled in the middle and four $\Phi 6.4$ mm holes in each corner with hole spacing of 72.8 mm. To pattern the grating Cu film on the stator, the detailed manufacturing process is as following and indicated in Fig. S1a. First, the surface of the stator acrylic board was covered by Cu film and PET (polyethylene terephthalate) film in order. The mask was patterned by CO₂ laser (Universal Laser Systems PLS6MW) to PET. Once the patterning process is completed, unused part of PET was stripped immediately and then cleaned by anhydrous ethanol. The stator was immersed in the PCB (printed circuit board) etchant solution for 12 h to fully react and then washed with anhydrous ethanol and deionized water. After peeling off the remaining PET film, PTFE (Polytetrafluoroethylene) film was covered on the stator to act as triboelectric material. The rotor panel of TENG is a transparent acrylic board with size of $\Phi 71 \times 3$ mm, a $\Phi 12.2$ mm hole of drilled in center. It was treated by the same etching process used by stator without PTFE film.

2.2. Characterization and measurement

The scanning electrons microscopy (SEM) images were acquired by a

field emission scanning electron microscope (JSM-6701 F, JEOL) to investigate the surface morphologies of PTFE film and Cu film. A stepper motor (Oriental Motor BX5120-A2) is used to drive TENG and controlled by motor driver (Oriental Motor BXSD120-C), as shown in Fig. S2a. The outputs of TENG were measured by Keithley 6514 electrometer and analyzed by National Instruments USB-6363 multifunction I/O device, as shown in Fig. S2b. Real-time data acquisition is implemented by programming NI-DAQmx interface and LabVIEW Runtime engine.

3. Results and discussions

Fig. 1 presents the structural assembly of bi-directional backstop triboelectric nanogenerator (BB-TENG), which can be approximated as a sandwich structure. It comprises two energy output unit called TENG-A and TENG-B, central bi-directional backstop rotation unit and four bolts for fastening overall structure and ensuring close contact between triboelectric surfaces, and it is almost flipped symmetrical along the central horizontal plane, as shown in Fig. 1a. The real photograph of BB-TENG is exhibited in Fig. S3. Fig. 1b shows the schematic diagram of the single backstop unit involved in this work, where one of the four inner pawls is uncovered to show its rotating mechanism. There are 50 ratchet teeth with a depth of 1 mm and a height of 3 mm around the circumference of the teeth shell. Four pawls, slightly thicker than the turntable, are correspondingly installed on four pawl shafts, and their covers are fixed to prevent the pawls from falling out. Each pawl is wrapped by its surrounding angle limiter, so pawls can only rotate within a restricted angle range around their shafts. Fig. S4 shows the photograph of the single backstop unit. The complete bi-directional backstop consists of a D-shaft, a spacer, and two identical backstop units. Through its symmetrical structure, as shown in Fig. S5, this bi-directional backstop implements one-way rotation on each side. Both TENG-A and TENG-B have the same rotary free-standing mode structure. The photographs of the stator and rotor of one TENG unit used in this work are shown in Fig. 1c. Fig. 1d-e display the SEM images of PTFE and Cu surfaces, these flat surfaces of two materials provide the conditions for good contact electrification.

When the D-shaft rotates counterclockwise, as shown in Fig. 2a(i), the bottom shell is locked by inner pawls and rotated synchronously in the same direction, while the top shell does not rotate. Fig. 2b(i) and (ii) explain the progress occurring inside the shell. At the beginning of rotation, the four pawls are affected by centrifugal force and surface friction force from turntable, resulting in that they will rotate clockwise along the corresponding pawl shafts and fall into the gap of two ratchet teeth. After that, D-shaft continues to rotate, the pawls in bottom shell are constrained by the radial resistance f (as denoted in Fig. 2b(ii)) from angle limiters and engage with ratchet teeth, thereby driving the bottom shell to rotate counterclockwise synchronously. When the D-shaft changes its rotation direction from counterclockwise to clockwise, as shown in Fig. 2a(i) to (iii), the bottom teeth shell will stop immediately and then the top shell begins to rotate. At the same time, the pawls in bottom teeth shell are also in motion, however, angle limiters restrict the rotation angle loosely in the opposite direction, in which case the pawls in top teeth shell can slide to the position of next ratchet tooth and repeat the above process. This movement process of pawls is presented in Fig. 2b(iii) to (i). The above-described process explains how bi-directional backstop rotates unidirectionally in the clockwise and counterclockwise directions, respectively.

Fig. 3a shows the operation of the freestanding mode TENG. Initially, the surfaces of PTFE and Cu were not charged before they contact. According to the triboelectric series, as illustrated in Fig. 3a(i), PTFE attracts electrons from Cu on the rotor, thus contact electrification-induced negative charges are generated and accumulated on PTFE film and the overlapping electrodes [35]. For the non-overlapping electrodes, they are charged in positive by PTFE. Once the Cu layers on rotor point at the gaps of stator electrodes, the rotor induces negative

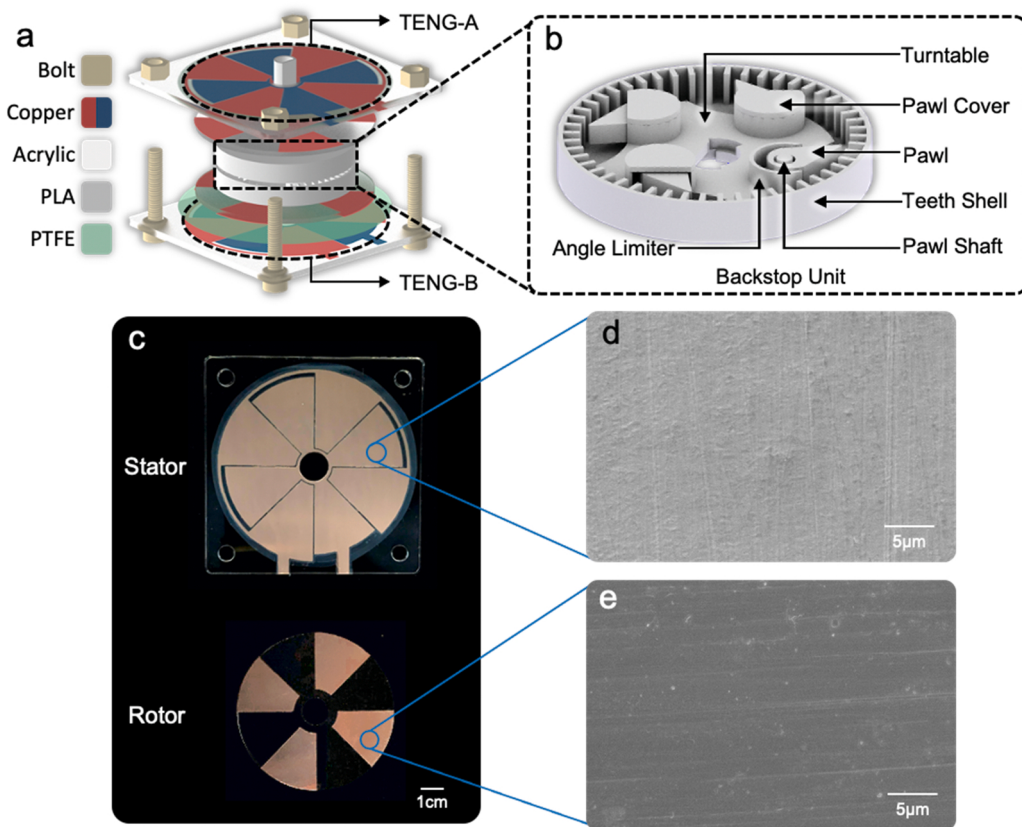


Fig. 1. Mechanical assembly and structural design of the BB-TENG. (a) Schematic diagram of BB-TENG from top to bottom, including TENG-A, a pair of backstops and TENG-B. (b) Detailed schematic diagram of the structure of a single backstop, consisting of a turntable, four pairs of pawl and pawl cover (for display reason, one pawl cover is not rendered) and a base. (c) Photograph of BB-TENG rotor and stator used in this work. SEM images of PTFE film (d) and Cu film (e).

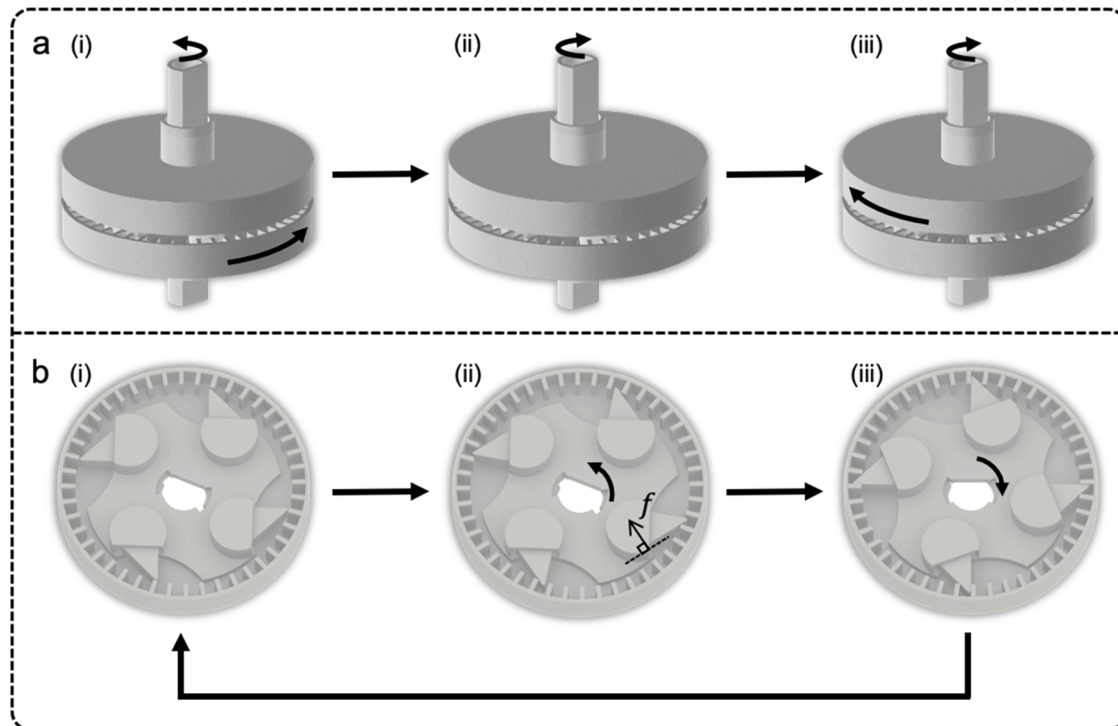


Fig. 2. Operating principle of the bi-directional backstop. The movement process of (a) bi-directional backstop and (b) inner pawls in the bottom backstop unit when the D-shaft rotates from counterclockwise to clockwise.

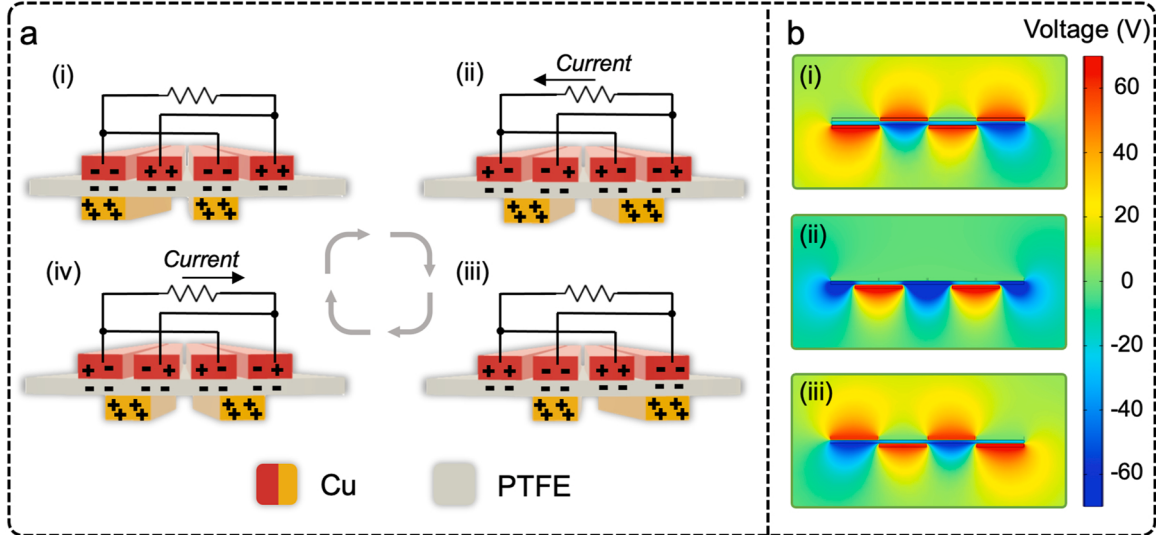


Fig. 3. Operating principle of the BB-TENG. (a) Illustrations of the working principle of single TENG unit under short-circuit condition. (b) Electric field simulation of BB-TENG by COMSOL in three different states.

charges on each overlapping electrode, while positive charges are generated on the non-overlapping areas of electrodes behind PTFE to rebuild charge equilibrium, as shown in Fig. 3a(ii). With continuing motion, the rotor induces an opposite result on the electrodes (see Fig. 3a(iii) to (iv)). As the rotor rotates, free electrons transfer between internal electrodes through external circuit, resulting in an AC current periodically. In addition, the in-plane simulation results obtained using COMSOL are adopted to elucidate the working principle of BB-TENG to derive a more quantitative understanding of the proposed voltage-generating process. Fig. 3b shows the electric potential distributions induced by conductive surface and adjacent charge in three states. When the top electrodes are fully aligned with the bottom Cu sector on rotor, the electric potential reaches a maximum value as shown

in Fig. 3b(i) and (iii). When the gaps of top electrodes fully overlap with the bottom Cu sector, Fig. 3b(ii) demonstrates that the electric potential between them is almost zero. The PTFE film always has a negative electrical potential due to its electret material.

To characterize the electrical output performance of the BB-TENG, a stepper motor test system controlled by motor driver is established to perform output measurement of TENG-A under different conditions, and the results are illustrated in Fig. 4. First, the rotor-stator area ratio is defined by $\eta = \theta' / \theta$, where θ' and θ are the angles of the sector Cu film on the rotor and stator, respectively, as shown in Fig. S6, and the TENG output curve characteristics are compared for different η values by changing θ' . As shown in Fig. 4a, the open-circuit voltage V_{oc} behaves as a square wave when η is 0.25. This is because the angle of Cu film on

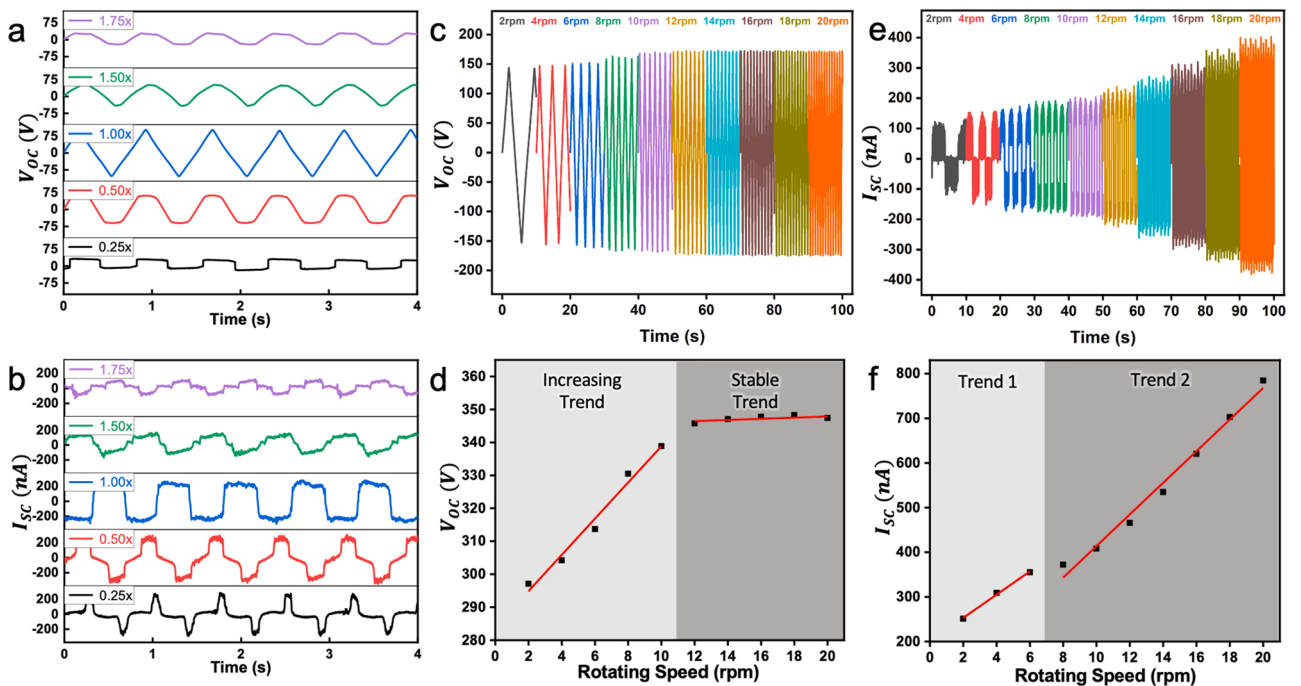


Fig. 4. Electrical output characterization of TENG-A in the BB-TENG. (a) The open-circuit voltage V_{oc} and (b) the short-circuit current I_{sc} of TENG-A with different rotor-stator area ratio η . (c) V_{oc} and (e) I_{sc} of TENG-A under different rotating speeds (2–20 rpm). Fitting relationships between rotating speed and (d) peak-to-peak V_{oc} and (f) peak-to-peak I_{sc} .

rotor is much smaller than that on stator, and its overlapping area remains constant for a period after the rotor and stator completely overlap, making no charge transfer between the electrodes. As η increases to 1.00, the complete overlap of rotor and stator occurs only for an instant, and the uniform angular change causes a uniform change in the overlapping area, so V_{oc} changes to a sharp triangular wave. Once η is larger than 1.00, the overlapping area will always exist, which prevents the interface between triboelectric materials from completely separating, resulting in irregular and meaningless V_{oc} outputs. Fig. 4b shows that the short-circuit current I_{sc} is fully consistent with the differentiation results of V_{oc} and is directly related to η . This experimental result matches with the theoretical calculation which verifies its correctness [36]. And it points out the condition for the BB-TENG to be used as a rotation sensor, i.e., the rotor-stator area ratio η must be 1.00, so that its V_{oc} waveform can reflect the motion state.

Fig. S7a and Fig. S7b show the output of V_{oc} and I_{sc} measured by the

electrometer when the TENG-A with an area ratio η of 1.00 is rotated at 20 rpm, respectively. Insets are enlarged views of the signals. It can be clearly seen from the magnified images that the V_{oc} has a high linearity during rotation, the value of I_{sc} looks like a significant pulse, and both are periodic in nature. The flat surfaces of Cu and PTFE films are the foundations for these well electrical signals. As the rotational speed increases from 2 to 20 rpm, V_{oc} increases from 143.46 V to 174.45 V and the maximum I_{sc} reaches 403.08 nA at 20 rpm, as illustrated in Fig. 4c and Fig. 4e. Besides, the corresponding peak-to-peak values of V_{oc} and I_{sc} both show two trends, but only the second trend of V_{oc} is stable and the others maintain increasing almost continuously. That means V_{oc} and I_{sc} exhibit a non-proportional relationship with rotation speed. According to the theory of freestanding mode TENG, TENG-A can be considered as a capacitor with constant transfer of charge through its two electrodes [36,37]. The V_{oc} of TENG-A has a closely relationship with the transferred charges, which depends on the overlapping area between two

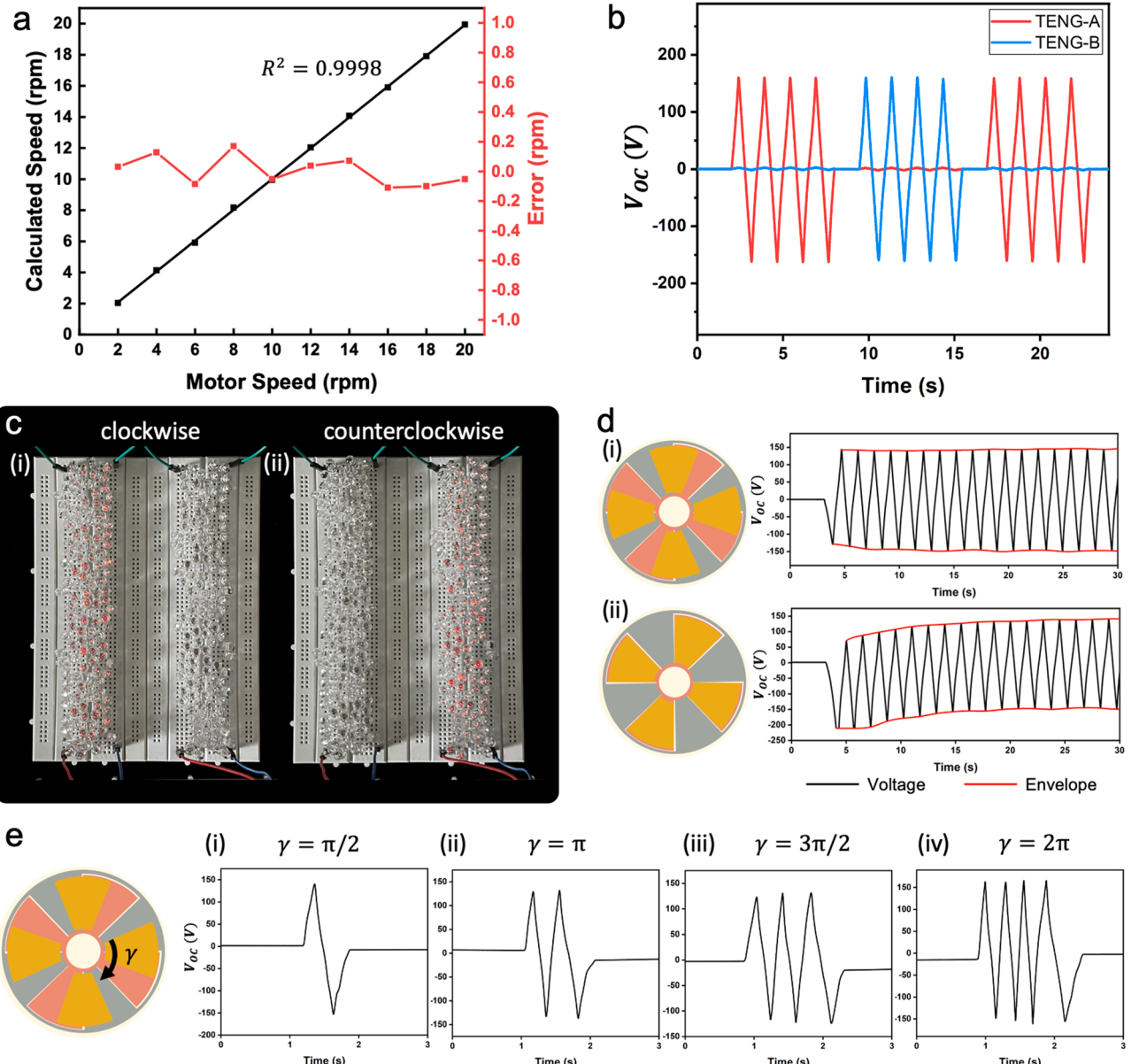


Fig. 5. Independent outputs and signal characteristics of BB-TENG. (a) Calculated rotating speed and error compared to the actual speed of stepper motor. (b) Synchronous V_{oc} of BB-TENG from two channels under alternately clockwise and counterclockwise rotating. (c) The picture of lighted LED arrays powered by BB-TENG rotating in different directions taken in daylight. (d) V_{oc} of TENG-A under different initial phases. (e) Measured V_{oc} of TENG-A when BB-TENG rotates clockwise (i) $\pi/2$, (ii) π , (iii) $3\pi/2$, (iv) 2π rad from initial position, respectively.

triboelectric layers in vertical direction. This explains why the V_{oc} output becomes stable after a linear increase, as exhibited in Fig. 4d. This is because when the rotation speed reaches 12 rpm, the rate of triboelectric charge generation is already higher than the rate of dissipation to the external environment, satisfying the condition of the maximum voltage output for TENG-A to behave as a constant capacitor. For result of I_{sc} shown in Fig. 4f, the first trend is due to the discrete movement characteristics of stepper motor. As shown in Fig. S8, I_{sc} can be thought as a series of pulsed currents distributed over each short time interval when TENG-A is rotating at a low speed. This results that it does not have high current outputs in large-scaled time. When the stepper motor is out of the range of low-speed rotation (0–7 rpm), its discrete motion turns to continuous motion and makes the rotation of TENG-A coherent, thus obtaining a linear change in the second trend. Fig. S9 displays the output performances of TENG-B, which have similar characteristics to TENG-A. In addition, the device durability was examined over 16,000 cycles. As shown in Fig. S10, the amplitude of transferred charges Q_{sc} between two Cu electrodes of TENG-A decreases slightly at first, and then remains stable for a long time. Meanwhile, during the whole testing process, the waveform shape of Q_{sc} remains unchanged and always keeps sharp. This illustrates the lifetime reliability of BB-TENG used as an angle vector sensor.

By further analyzing the output characteristics of BB-TENG, its inherent unique characteristics can be obtained. First, since the output voltage of the TENG is strongly correlated with rotation, this periodic relationship needs to be expressed quantitatively. According to the properties of the freestanding disc shaped TENG, the crest points of V_{oc} must occur at the moment when triboelectric surfaces on rotor and electrodes are fully aligned [38]. Also, in a short time interval, the motion of TENG can be regarded as uniform rotational motion, so a pair of local extreme points of the half-period are chosen as the starting and ending points as presented in Fig. S11 to calculate the time of one period. Thus, the rotation speed can be calculated. As shown in Fig. 5a, the calculated rotation speed is almost linearly distributed with a coefficient of determination R^2 of 0.9998. The error after subtracting the motor speed is distributed in a very minor scope, with maximum errors of no more than 0.2 rpm. Fig. 5b shows that in the case of alternating clockwise and counterclockwise rotation, the outputs of the two TENGs are independent and do not interfere with each other. This becomes the foundation for the rotational direction measurement that can be performed by the BB-TENG. To further demonstrate the dual-channel independent output capability of the BB-TENG, it is connected to two groups of 120 series-connected LEDs through full bridge rectifiers respectively, and the used circuit is shown in Fig. S12. In the experiment, the lighted state of two LED arrays can be controlled directly only by the rotation direction of BB-TENG, while without any external hardware or software logic components (Fig. 5c and Movie S1). Thus, the lighted state of two LED arrays can clearly reveal the rotation direction.

Supplementary material related to this article can be found online at doi:10.1016/j.nanoen.2022.107430.

To investigate the phase of BB-TENG in relation to the output of V_{oc} , firstly, the initial phase of the rotor is set in two positions, whether it is completely coincident with one electrode or not, e.g., 0 and $\pi/8$, respectively. As plotted in Fig. 5d, after 30 s of continuous clockwise rotation from the initial state, V_{oc} exhibits the same peak-to-peak voltage under the different stator initial phases, that is, the relative values of positive and negative voltage are same. However, the different initial phases lead to different trends. From the envelope (denoted in Fig. 5d), the V_{oc} trend is stable when the stator is uniformly overlapped with two electrodes. And when the stator is exactly overlapped with one electrode, the V_{oc} goes through a bending process. This implies that the absolute value of the BB-TENG output is not fixed, but the information needs to be extracted by further analyzing the waveform shape. Furthermore, the relationship between V_{oc} waveform and rotation angle of BB-TENG was investigated under the initial condition of steady state.

Fig. 5e shows V_{oc} outputs of BB-TENG when it rotates clockwise by $\pi/2$, π , $3\pi/2$ and 2π rad, respectively. The number of crest pair of V_{oc} increases linearly with the rotation angle, so a conclusion can be inferred that every time the V_{oc} waveform encounters a crest pair, it means that the BB-TENG has rotated $\pi/2$ rad. By reducing the angle of each triboelectric layer and electrode, the resolution of rotation can be further improved.

Aiming to explore the deep application of BB-TENG as a self-driven sensor in IoT field, a passcode dialer was designed as shown in the inset image of Fig. 6a. It works as a human-machine interface for converting motional angle to digital information, and a digital signal processing (DSP) system was designed for security verification. As the schematic illustration in Fig. 6a, BB-TENG is installed on the door and its two TENGs are connected to electrostatic meters where their signals are analyzed, presented, and controlled by the DSP system. The different signal sequences generated by the manual rotation of BB-TENG lead to different analysis results and whether to lock the door or not. Assuming that the letters 'r' and 'b' are used to denote the two rotation directions respectively, the built-in passcode used for testing is noted as "2r3b1b1r". To extract the original angle information from the signal, a primitive signal processing logic (Fig. S13a) is designed to analyze the process that the DSP architecture should contain. Based on the logic diagram, it was determined that the peak-seeking algorithm mainly consists of digital sampling, differencing, threshold square signal resampling and edge triggering, as shown in Fig. S13b, and the processing results of built-in passcode of each process are shown in Fig. 6b–e respectively. This algorithm has been applied to the V_{oc} output with different trends in Fig. 5d, as shown in Fig. S14, and the peek signals processed using this algorithm are not affected by the magnitude of the V_{oc} . Once the normalized logic signal output through the peak-seeking algorithm is obtained, the rotation sequence can be reconstructed by means of the finite state machine represented in Fig. S15, and each number represents the occurrence number of $\pi/2$ rad or crest pairs. To verify the reliability of the passcode dialer, a set of comparison experiments with the same angle sequence but different directions were designed (Movie S2). First, the administrator rotated the correct built-in passcode, then the identity was successfully verified by DSP system and permission is granted, as shown in Fig. 6f. Subsequently, the hacker obtained the numerical password through attack methods and tried to enter the system but could not get the correct direction information. In Fig. 6g, hacker rotated the passcode with wrong directions, so the security system can detect these differences and deny every risky attempt. These results not only illustrate the ability of the BB-TENG to perform both angle and direction sensing, but further demonstrate the enhanced security aspects of passcode devices based on it, providing a broad prospect for practical applications of rotation sensing in IoT field.

Supplementary material related to this article can be found online at doi:10.1016/j.nanoen.2022.107430.

4. Conclusions

In conclusion, we have developed a self-driven angle vector sensor to monitor both angle and direction of rotation. The unique bi-directional backstop rotation structure enables BB-TENG to measure in each direction individually. It also has an optimized size and structural design to expand its application in space-constrained scenarios. During the study of the rotor-stator ratio, it was found that the parameter η can significantly determine the output signal waveform of TENG and is consistent with the theoretical calculation of this free-standing mode. This is the foundation for further analyzing the BB-TENG output signal. With the unique performance of the BB-TENG, an output voltage of 174.45 V, high voltage output signal and configurable sensitivity are achieved when sensing external rotation. By calculating crest periods of V_{oc} , the real-time rotation speed can be measured by BB-TENG in the range of 2–20 rpm with a maximum error of 0.2 rpm. In addition, a signal processing algorithm is proposed to analyze and reconstruct the

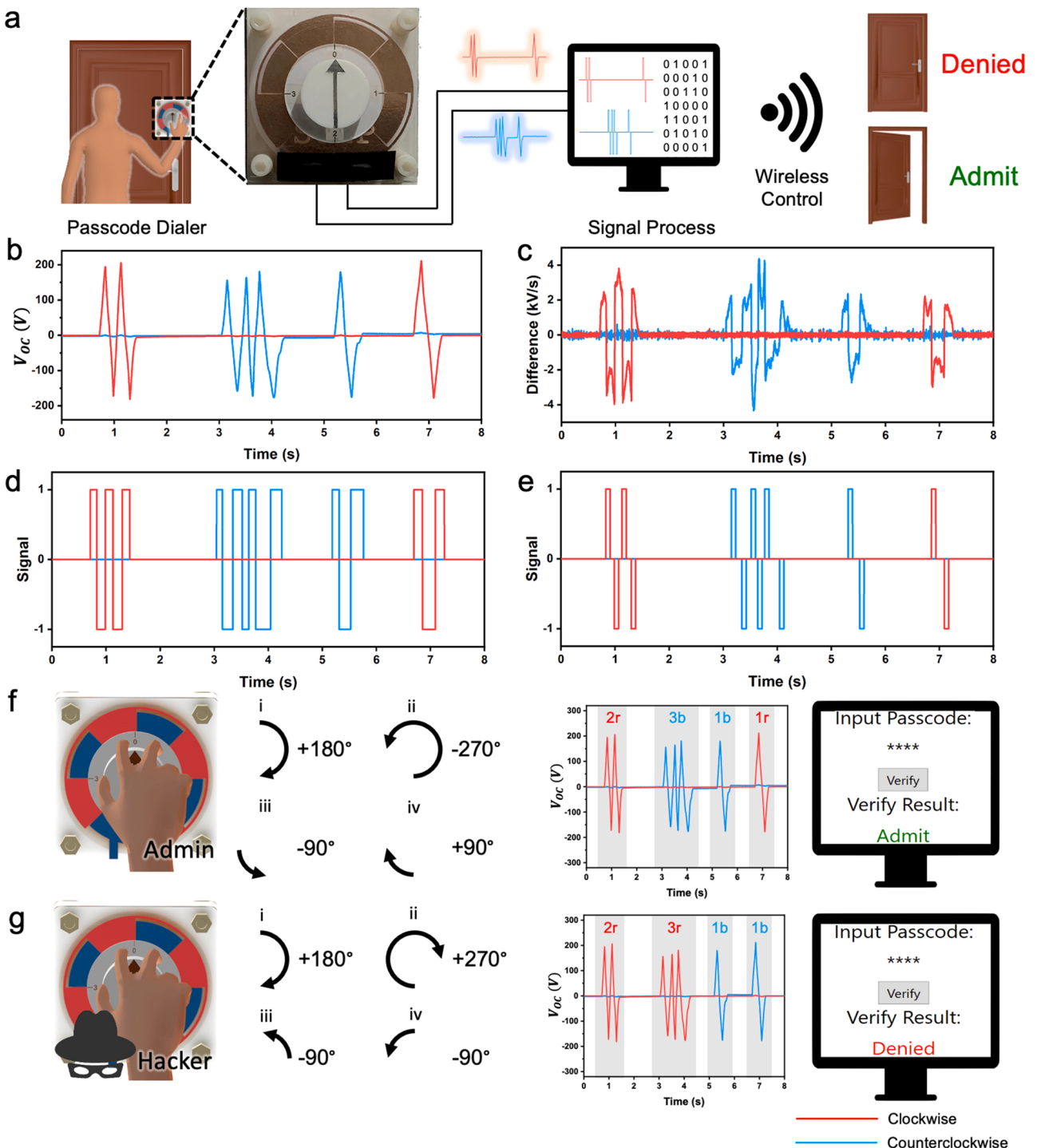


Fig. 6. Application of BB-TENG and signal processing algorithm. (a) Schematic diagram of passcode dialer based on BB-TENG, which is applied on human-machine password verification. Dual-channel open-circuit voltage V_{oc} (b), different analog signals(c), different digital signals(d) and logical peek signals of BB-TENG with correct order passcode “2r3b1b1r”. Rotation sequence, output voltage and validation result of (f) correct order “2r3b1b1r” and (g) wrong order “2r3r1b1b”.

original rotation angle information without the influence of initial phase. In addition, a self-driven passcode dialer based on BB-TENG are demonstrated as a practical application, which will greatly enhance the robustness of the password input devices. This sensor design that fully reproduces rotation information is a promising strategy in the future for widely used self-powered IoT monitoring devices.

CRediT authorship contribution statement

Wenchi Hou: Conceptualization, Methodology, Visualization, Data curation, Writing – original draft. **Xiaolong Tang:** Visualization, Validation. **Lin Fang:** Data curation, Validation. **Qiwei Zheng:** Methodology, Validation. **Xiangyu Chen:** Resources, Conceptualization, Methodology. **Li Zheng:** Resources, Conceptualization, Methodology, Supervision, Writing – review & editing.

Declaration of Competing Interest

The authors declare that they have no known competing financial interests or personal relationships that could have appeared to influence the work reported in this paper.

Acknowledgements

The work was supported by National Key R&D Project from Minister of Science and Technology (2021YFA1201601), the National Natural Science Foundation of China (Grant No. 62174014), Beijing Nova Program (Z201100006820063) and Youth Innovation Promotion Association CAS (2021165), the Program for Professor of Special Appointment (Eastern Scholar) (TP2017076) at Shanghai Institutions of Higher Learning, and Science and Technology Commission of Shanghai Municipality (19DZ2271100).

Appendix A. Supporting information

Supplementary data associated with this article can be found in the online version at [doi:10.1016/j.nanoen.2022.107430](https://doi.org/10.1016/j.nanoen.2022.107430).

References

- [1] A.S.A. Kumar, B. George, S.C. Mukhopadhyay, Technologies and applications of angle sensors: a review, *IEEE Sens. J.* 21 (2021) 7195–7206, <https://doi.org/10.1109/JSEN.2020.3045461>.
- [2] M. Benamar, A.S.P. Gonzales, A new fast tracking resolver for mechanical angle measurement, 2013 Africon, IEEE, Pointe-Aux-Piments, Mauritius (2013) 1–4, <https://doi.org/10.1109/AFRCON.2013.6757717>.
- [3] H.-J. Sheng, G.-R. Lin, P.-T. Tsai, C.-A. Yang, M.-H. Kuo, H.-T. Sun, M.-Y. Fu, W.-F. Liu, Random-rotational angle sensor based on fiber Bragg gratings, in: 2012 17th Opto-Electronics and Communications Conference, IEEE, Busan, Korea (South), 2012, pp. 192–193. <https://doi.org/10.1109/OECC.2012.6276436>.
- [4] C. Giebelner, D.J. Adelerhof, A.E.T. Kuiper, J.B.A. van Zon, D. Oelgeschläger, G. Schulz, Robust GMR sensors for angle detection and rotation speed sensing, *Sens. Actuators A Phys.* 91 (2001) 16–20, [https://doi.org/10.1016/S0924-4247\(01\)00510-6](https://doi.org/10.1016/S0924-4247(01)00510-6).
- [5] X.D. Zhang, L.Y. Kang, W.F. Diao, The principle of the potentiometer and its applications in the vehicle steering, in: IEEE International Conference on Vehicular Electronics and Safety, 2005, IEEE, Xi'an, China, 2005, pp. 20–24. <https://doi.org/10.1109/ICVES.2005.1563607>.
- [6] A. Whitmore, A. Agarwal, L. Da Xu, The Internet of Things—a survey of topics and trends, *Inf. Syst. Front.* 17 (2015) 261–274, <https://doi.org/10.1007/s10796-014-9489-2>.
- [7] A. Čolaković, M. Hadžalić, Internet of Things (IoT): a review of enabling technologies, challenges, and open research issues, *Comput. Netw.* 144 (2018) 17–39, <https://doi.org/10.1016/j.comnet.2018.07.017>.
- [8] F.R. Fan, Z.Q. Tian, Z. Lin Wang, Flexible triboelectric generator, *Nano Energy* 1 (2012) 328–334, <https://doi.org/10.1016/j.nanoen.2012.01.004>.
- [9] P. Wang, L. Pan, J. Wang, M. Xu, G. Dai, H. Zou, K. Dong, Z.L. Wang, An ultra-low-friction triboelectric-electromagnetic hybrid nanogenerator for rotation energy harvesting and self-powered wind speed sensor, *ACS Nano* 12 (2018) 9433–9440, <https://doi.org/10.1021/acsnano.8b04654>.
- [10] J. Zhong, Q. Zhong, F. Fan, Y. Zhang, S. Wang, B. Hu, Z.L. Wang, J. Zhou, Finger typing driven triboelectric nanogenerator and its use for instantaneously lighting up LEDs, *Nano Energy* 2 (2013) 491–497, <https://doi.org/10.1016/j.nanoen.2012.11.015>.
- [11] Q. Tang, M.-H. Yeh, G. Liu, S. Li, J. Chen, Y. Bai, L. Feng, M. Lai, K.-C. Ho, H. Guo, C. Hu, Whirligig-inspired triboelectric nanogenerator with ultrahigh specific output as reliable portable instant power supply for personal health monitoring devices, *Nano Energy* 47 (2018) 74–80, <https://doi.org/10.1016/j.nanoen.2018.02.039>.
- [12] X. Liu, P. Cui, J. Wang, W. Shang, S. Zhang, J. Guo, G. Gu, B. Zhang, G. Cheng, Z. Du, A robust all-inorganic hybrid energy harvester for synergistic energy collection from sunlight and raindrops, *Nanotechnology* 32 (2021), 075401, <https://doi.org/10.1088/1361-6528/ab84b>.
- [13] Z.L. Wang, Nanogenerators, self-powered systems, blue energy, piezotronics and piezo-phototronics – a recall on the original thoughts for coining these fields, *Nano Energy* 54 (2018) 477–483, <https://doi.org/10.1016/j.nanoen.2018.09.068>.
- [14] Z.L. Wang, Triboelectric Nanogenerator (TENG)—sparking an energy and sensor revolution, *Adv. Energy Mater.* 10 (2020) 2000137, <https://doi.org/10.1002/aenm.202000137>.
- [15] Z.L. Wang, Triboelectric nanogenerators as new energy technology for self-powered systems and as active mechanical and chemical sensors, *ACS Nano* 7 (2013) 9533–9557, <https://doi.org/10.1021/nn404614z>.
- [16] Y. Liu, J. Mo, Q. Fu, Y. Lu, N. Zhang, S. Wang, S. Nie, Enhancement of triboelectric charge density by chemical functionalization, *Adv. Funct. Mater.* 30 (2020) 2004714, <https://doi.org/10.1002/adfm.202004714>.
- [17] H. Zou, Y. Zhang, L. Guo, P. Wang, X. He, G. Dai, H. Zheng, C. Chen, A.C. Wang, C. Xu, Z.L. Wang, Quantifying the triboelectric series, *Nat. Commun.* 10 (2019) 1427, <https://doi.org/10.1038/s41467-019-10946-1>.
- [18] W. Shang, G. Gu, W. Zhang, H. Luo, T. Wang, B. Zhang, J. Guo, P. Cui, F. Yang, G. Cheng, Z. Du, Rotational pulsed triboelectric nanogenerators integrated with synchronously triggered mechanical switches for high efficiency self-powered systems, *Nano Energy* 82 (2021), 105725, <https://doi.org/10.1016/j.nanoen.2020.105725>.
- [19] Q. Zheng, L. Fang, X. Tang, L. Zheng, H. Li, Indoor air dust removal system based on high-voltage direct current triboelectric nanogenerator, *Nano Energy* 97 (2022), 107183, <https://doi.org/10.1016/j.nanoen.2022.107183>.
- [20] J. Mo, C. Zhang, Y. Lu, Y. Liu, N. Zhang, S. Wang, S. Nie, Radial piston triboelectric nanogenerator-enhanced cellulose fiber air filter for self-powered particulate matter removal, *Nano Energy* 78 (2020), 105357, <https://doi.org/10.1016/j.nanoen.2020.105357>.
- [21] C. Wu, H. Huang, S. Yang, G. Wen, Pagoda-shaped triboelectric nanogenerator with high reliability for harvesting vibration energy and measuring vibration frequency in downhole, *IEEE Sens. J.* 20 (2020) 13999–14006, <https://doi.org/10.1109/JSEN.2020.3007000>.
- [22] L. Fang, Q. Zheng, W. Hou, L. Zheng, H. Li, A self-powered vibration sensor based on the coupling of triboelectric nanogenerator and electromagnetic generator, *Nano Energy* 97 (2022), 107164, <https://doi.org/10.1016/j.nanoen.2022.107164>.
- [23] W. Li, D. Torres, R. Díaz, Z. Wang, C. Wu, C. Wang, Z. Lin Wang, N. Sepúlveda, Nanogenerator-based dual-functional and self-powered thin patch loudspeaker or microphone for flexible electronics, *Nat. Commun.* 8 (2017) 15310, <https://doi.org/10.1038/ncomms15310>.
- [24] J. Wang, W. Ding, L. Pan, C. Wu, H. Yu, L. Yang, R. Liao, Z.L. Wang, Self-powered wind sensor system for detecting wind speed and direction based on a triboelectric nanogenerator, *ACS Nano* 12 (2018) 3954–3963, <https://doi.org/10.1021/acsnano.8b01532>.
- [25] J. Liao, Y. Zou, D. Jiang, Z. Liu, X. Qu, Z. Li, R. Liu, Y. Fan, B. Shi, Z. Li, L. Zheng, Nestable arched triboelectric nanogenerator for large deflection biomechanical sensing and energy harvesting, *Nano Energy* 69 (2020), 104417, <https://doi.org/10.1016/j.nanoen.2019.104417>.
- [26] S. Zhang, J. Guo, L. Liu, H. Ruan, C. Kong, X. Yuan, B. Zhang, G. Gu, P. Cui, G. Cheng, Z. Du, The self-powered artificial synapse mechanotactile sensing system by integrating triboelectric plasma and gas-ionic-gated graphene transistor, *Nano Energy* 91 (2022), 106660, <https://doi.org/10.1016/j.nanoen.2021.106660>.
- [27] D. Choi, T. Sung, J. Kwon, A self-powered smart roller-bearing based on a triboelectric nanogenerator for measurement of rotation movement, *Adv. Mater. Technol.* 3 (2018) 1800219, <https://doi.org/10.1002/admt.201800219>.
- [28] X.H. Li, C.B. Han, T. Jiang, C. Zhang, Z.L. Wang, A ball-bearing structured triboelectric nanogenerator for nondestructive damage and rotating speed measurement, *Nanotechnology* 27 (2016), 085401, <https://doi.org/10.1088/0957-4484/27/8/085401>.
- [29] Y. Wu, Q. Jing, J. Chen, P. Bai, J. Bai, G. Zhu, Y. Su, Z.L. Wang, A self-powered angle measurement sensor based on triboelectric nanogenerator, *Adv. Funct. Mater.* 25 (2015) 2166–2174, <https://doi.org/10.1002/adfm.201403828>.
- [30] C. Li, Z. Wang, S. Shu, W. Tang, A self-powered vector angle/displacement sensor based on triboelectric nanogenerator, *Micromachines* 12 (2021) 231, <https://doi.org/10.3390/mi12030231>.
- [31] J. Chen, H. Guo, C. Hu, Z.L. Wang, Robust triboelectric nanogenerator achieved by centrifugal force induced automatic working mode transition, *Adv. Energy Mater.* 10 (2020) 2000886, <https://doi.org/10.1002/aenm.202000886>.
- [32] X. Lu, H. Zhang, X. Zhao, H. Yang, L. Zheng, W. Wang, C. Sun, Triboelectric nanogenerator based self-powered sensor with a turnable sector structure for monitoring driving behavior, *Nano Energy* 89 (2021), 106352, <https://doi.org/10.1016/j.nanoen.2021.106352>.
- [33] S.M.S. Rana, M.A. Zahed, M.T. Rahman, M. Salauddin, S.H. Lee, C. Park, P. Mahajan, T. Bhatta, K. Shrestha, J.Y. Park, Cobalt-nanoporous carbon functionalized nanocomposite-based triboelectric nanogenerator for contactless and sustainable self-powered sensor systems, *Adv. Funct. Mater.* 31 (2021) 2105110, <https://doi.org/10.1002/adfm.202105110>.
- [34] D. Bhatia, S.H. Jo, Y. Ryu, Y. Kim, D.H. Kim, H.-S. Park, Wearable triboelectric nanogenerator based exercise system for upper limb rehabilitation post neurological injuries, *Nano Energy* 80 (2021), 105508, <https://doi.org/10.1016/j.nanoen.2020.105508>.
- [35] G. Zhu, J. Chen, T. Zhang, Q. Jing, Z.L. Wang, Radial-arrayed rotary electrification for high performance triboelectric generator, *Nat. Commun.* 5 (2014) 3426, <https://doi.org/10.1038/ncomms4426>.
- [36] T. Jiang, X. Chen, C.B. Han, W. Tang, Z.L. Wang, Theoretical study of rotary freestanding triboelectric nanogenerators, *Adv. Funct. Mater.* 25 (2015) 2928–2938, <https://doi.org/10.1002/adfm.201500447>.
- [37] J. Wang, W. Ding, L. Pan, C. Wu, H. Yu, L. Yang, R. Liao, Z.L. Wang, Self-powered wind sensor system for detecting wind speed and direction based on a triboelectric nanogenerator, *ACS Nano* 12 (2018) 3954–3963, <https://doi.org/10.1021/acsnano.8b01532>.
- [38] L. Lin, S. Wang, Y. Xie, Q. Jing, S. Niu, Y. Hu, Z.L. Wang, Segmentally structured disk triboelectric nanogenerator for harvesting rotational mechanical energy, *Nano Lett.* 13 (2013) 2916–2923, <https://doi.org/10.1021/nl4013002>.